J. Fluid Mech. (2000), *vol.* 405, *pp.* 243–268. Printed in the United Kingdom

Shear flow over a self-similar expanding pulmonary alveolus during rhythmical breathing

By S. HABER[1]†, J. P. BUTLER[2], H. BRENNER[3], I. EMANUEL[1] AND A. TSUDA[2]

[1] Department of Mechanical Engineering, Technion, Haifa 32000, Israel

[2] Department of Environmental Health, Harvard School of Public Health, Boston, MA 02115, USA

[3] Department of Chemical Engineering, Massachusetts Institute of Technology, Cambridge, MA 02139–4307, USA

(Received 30 October 1996 and in revised form 9 June 1999)

Alternating shear flow over a self-similar, rhythmically expanding hemispherical depression is investigated. It provides a fluid-mechanical model for an alveolated respiratory unit, by means of which the effect of lung rhythmical expansion on gas mixing as well as aerosol dispersion and deposition can be studied. The flow is assumed to be very slow and governed by the quasi-steady linear Stokes equations. Consequently, superposition of the following two cases provides an easy route toward characterizing the aforementioned flow field. The first case treats the flow field that is generated by a rhythmically expanding spherical cap (the alveolus). The cap is attached at its rim to a circular opening in an expanding unbounded plane bounding a semi-infinite fluid region. The rate of expansion of the cap and the plane are chosen such as to maintain the system's configurational self-similarity. The second case addresses the flow disturbance that is generated by an alternating shear flow encountering a rigid hemispherical cavity in a plane bounding a semi-infinite fluid domain.

For the first case, a stream-function representation employing toroidal coordinates furnishes an analytical solution, whereas the second case was solved numerically by Pozrikidis (1994). Linear superposition of the two flow cases results in particularly rich streamline maps. In the symmetry plane (bisecting the cap and parallel to the mean shear flow), for a certain range of shear to expansion-rate ratios, the streamline maps are self-similar and display closed orbits and two internal stagnation points. One of the stagnation points is a 'centre' surrounded by closed streamlines whereas the other constitutes a 'saddle point'. For other planes, no stagnation points exist in the field, but the streamlines associated with the saddle point display complex looping patterns. These unique flow structures, when subjected to a small perturbation (e.g. a small asynchrony between ductal and alveolar entering flows) cause highly complex stochastic particle trajectories even in the quasi-static Stokes alveolar flow. The observed irreversible flow phenomena in a rhythmically expanding alveolus may be partially responsible for the 'stretch-and-fold' flow mixing patterns found in our recent flow visualization studies performed in excised animal lung acini.

† Author to whom correspondence should be addressed.

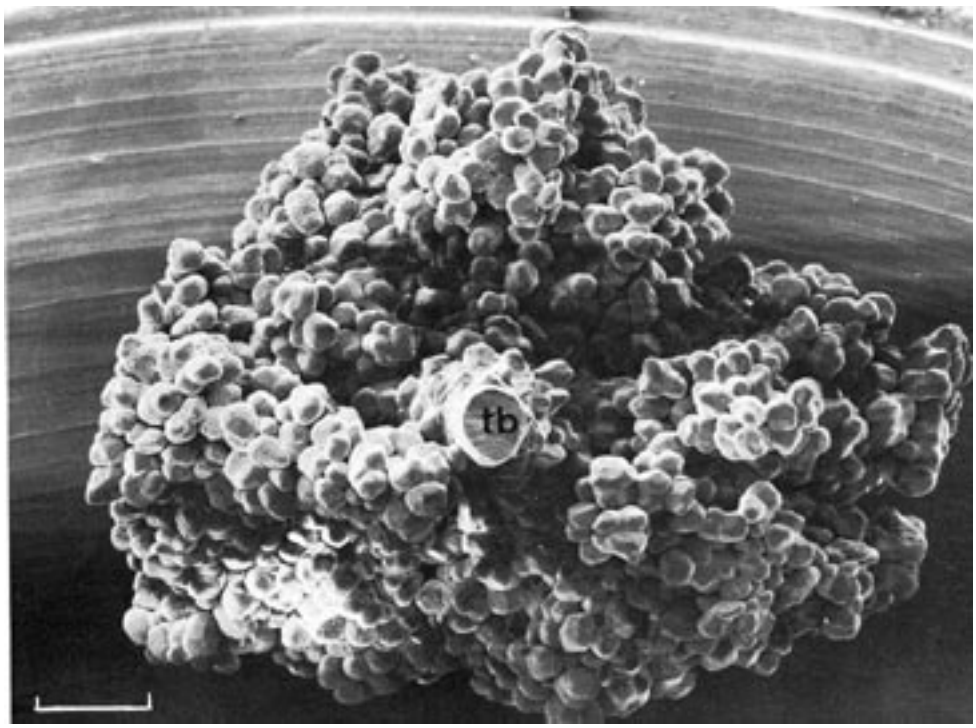

FIGURE 1. The pulmonary alveolated airways (Rodriguez *et al.* 1987).

1. Introduction

The fluid-dynamical problem addressed in this paper was motivated by the search for insight into transport phenomena occurring deep within the lungs. Though the backbone of the paper consists of an analytic investigation of a flow model of an expanding alveolus, the rationale behind its choice requires elucidation. Thus, two main themes govern this physiological introductory section. First, the physiological background leading to the mathematical model eventually employed is addressed. Second, a brief overview is provided of existing solutions of several closely related fluid dynamical problems.

Aerosol transport and deposition phenomena in the lung airways and terminal airspaces are governed both by the anatomy of the respiratory tract and by the local velocity field of the gas associated with rhythmical breathing. In the pulmonary acinus† (figure 1), the airways that become progressively more and more highly alveolated function in an expanding and contracting mode occasioned by breathing. Within the acinus, care must be taken to differentiate between the kinematic motion of the alveolar ducts and the alveoli proper. The former act as the terminal conduit for gas flow, whereas the latter are closed-end sacs bounded by the alveolar septa engaged in gas exchange. Typical length scales associated with ductal diameters and alveolar diameters are roughly the same, namely a few hundred microns, depending on species (although it is interesting to note that there exists only a very weak dependence of alveolar size on body mass as the latter ranges over some five orders

† The pulmonary acinus is the basic alveolar unit of the lung. Normally, alveolation occurs from around the 16th bifurcation of the respiratory tract (Haefeli-Bleuer & Weibel 1988).

of magnitude from shrew to elephant). Due to the very rapid increase of net bronchial cross-sectional area with distance down the tracheo-bronchial tree, linear velocities in the terminal air units are less than a few $cm\,s^{-1}$ in humans. As the kinematic viscosity of air is about $0.17\,cm^2\,s^{-1}$, this results in Reynolds number estimates of substantially less than unity. Accordingly, creeping-flow analyses are appropriate for flow in the pulmonary acinus.

During breathing, alveoli and alveolar ducts expand and contract in a manner roughly consistent with geometric similarity, namely all dimensions, apart from septal thickness, scale approximately as the $\frac{1}{3}$ power of lung volume. This fact has been shown in lung specimens fixed at a variety of lung volumes by intravascular perfusion (Gil & Weibel 1972; Gil *et al.* 1979; Weibel 1986), and with motion of pleural markers in unfixed preparations (Ardila, Horie & Hildebradt 1974). More recently, Miki *et al.* (1993) have shown that approximate geometric similarity exists in pulmonary surface-to-volume ratios in living animals, but that there is also a small but systematic degree of geometric hysteresis associated with breathing.

To date, apart from the gross effects of overall ventilation, little attention has been paid to the effect of velocity profiles within rhythmically expanding and contracting acini on gas exchange and aerosol deposition. In the case of gas exchange, the details of acinar flow are unlikely to be critical, since the time scale for diffusive transport in this region is of the order of a few milliseconds, which, being much faster than breathing periods, implies little effect of flow patterns per se on gas transport.

The case of aerosol transport, by contrast, is quite different. Here particles range in size from submicron to many microns. As such, they may cross streamlines and deposit on alveolar surfaces due to inertial crossing of curved streamlines, gravitational sedimentation or by Brownian motion (Brain, Blanchard & Sweeney 1989). Consequently, the fluid velocity profiles and concomitant streamline characteristics play a significant role in the fate of such particles. Tsuda, Butler & Fredberg (1994*a*, *b*) found that aerosol transport and deposition patterns were very sensitive to certain aspects of the alveolated geometry, including the ratio of alveolar to central channel volume, the opening size of the alveoli, and the alveolar surface area per unit volume. These authors analysed particle trajectories for the case of fine particles crossing streamlines under the influence of Brownian motion, and separately for larger aerosol particles undergoing gravitational sedimentation. These findings were later confirmed by a similar alveolar duct model (Darquenne & Paiva 1996).

With the exception of the investigations by Davidson & Fitz-Gerald (1972), Tsuda, Henry & Butler (1995*a*), and Tsuda, Otani & Butler (1999), the previous studies cited have focused almost entirely on elucidating velocity profiles or streamlines in rigid-walled structures, using a variety of architectural features to mimic the essential static geometric features of the pulmonary acinus. But as argued above, especially in the case of aerosol transport, the dynamic effects of periodic wall motion may play an important role in lung aerosol deposition phenomena. Accordingly the major goal of this paper is to characterize streamlines in a geometric model that captures the dual features central to acinar transport, namely periodic wall motion (that is approximately self-similar) and alternating shear flow within the alveolated ducts.

The pulmonary acinus depicted in figure 1 suggests that a single alveolus may be approximated geometrically by a spherical cap attached at its rim to the alveolar duct (see also Gil *et al.* 1979). If the alveolus diameter is smaller than that of the central duct, the model configuration can be further simplified to include a spherical cap attached at its rim to a flat surface (see figure 2), a geometric configuration which is tractable to analysis in toroidal coordinates. Moreover, even in cases where the

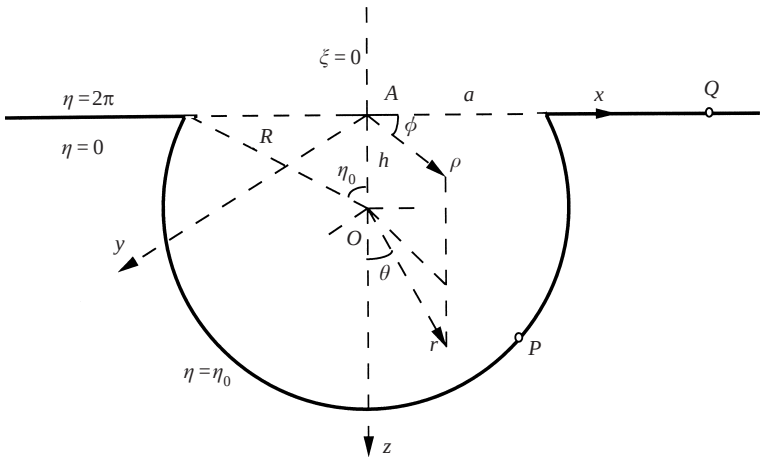

FIGURE 2. The spherical-cap model of a respiratory unit.

alveolus and duct diameters are of comparable size, use of this geometry promises that the flow structure inside the alveolus is likely to represent a more faithful portrayal of real events than in previous models. Even employing the full unsteady Navier–Stokes equations, Tsuda *et al.* (1995*a*) also obtained the result that the flow structure hardly changes with time. Accordingly, the quasi-static Stokes equations (Happel & Brenner 1983) provide an accurate description of the flow field. Under these conditions, linear superposition of the following two cases provides an easy route towards characterizing the flow field within a rhythmically expanding alveolar duct: Case A – the flow field generated by a rhythmically expanding alveolus; Case B – alternating shear flow over a plane wall containing a hemispherical depression.

A similar flow was analysed by Tsuda *et al.* (1995*a*), for an axisymmetric alveolar duct configuration and non-zero Reynolds number. The duct consisted of a centrally circular thoroughfare surrounded by a toroidal alveolus. It performed a reversible, oscillatory, self-similar stretching movement. The full Navier–Stokes equations were numerically solved to obtain the rhythmically expanding non-zero low-Reynolds-number flow field. Under certain conditions, a saddle point was found near the alveolar opening and pathlines in the alveolus exhibited chaotic features. It remained unclear whether the latter was due entirely to the non-zero, but small Reynolds number assumed by Tsuda *et al.* (1995*a*) or whether these effects would persist even in quasi-static Stokes flows. Accordingly, we are also interested in verifying whether chaotic pathlines appear in our zero-Reynolds-number flow model. If so, such knowledge would greatly simplify future research on the effect of the various phenomenological coefficients on the appearance of chaos, since Stokes flows are easier to analyse than unsteady Navier–Stokes flows.

Problems closely related to that of an expanding alveolus are encountered in a wide variety of applications to many fields of science and engineering. These include direct-contact heat exchange, liquid-membrane technology, bubble boiling phenomena, coalescence of living cells, and oil or raindrop coalescence.

Theoretical studies of particular interest in the present context are the works of Avedisian & Andres (1978) on the partially engulfing evaporation of a liquid drop, of Schneider, O'Neill & Brenner (1973) on the rotational motion generated by a partially immersed sphere, of Davis (1982) on the force exerted by a two-phase Stokes flow

on a sphere which symmetrically straddles the interface, of Vuong & Sadhal (1989) on the growth and translation of a liquid vapour compound drop, and of El-Kareh & Secomb (1996) who obtained an analytical solution for the flow impinging on a spherical cap on a plane wall. They employed toroidal coordinates and the Mehler–Fock transform (fully described in Sneddon 1972) that underlies the mathematical analysis to obtain creeping-flow solutions for various boundary configurations and conditions. An exact analytical solution that employs a stream function representation was first suggested by Payne & Pell (1960). A technique similar to that of Vuong & Sadhal (1989) was employed in the present work to solve case A, albeit with some significant modifications. Case B was addressed by Pozrikidis (1994) who applied a mixed analytical and numerical approach to obtain the shear flow over a rigid cavity in the form of a spherical cap.

The paper is divided into three parts. Section 2 treats case A of the flow generated by a rhythmically expanding alveolus. An analytical solution is obtained and the streamline pattern is calculated for various alveoli rim/plane angles η_0.

Section 3 addresses the combined effect of rhythmical expansion and alternating shear (cases A + B) and a streamline pattern is calculated for various values of expansion to shear-rates ratios.

Section 4 provides a brief discussion on the dynamical system governing the trajectories of massless particles immersed in the flow field of cases A + B for a hemispherical cavity. It also addresses the implications of the unique streamline maps in relation to possible chaotic trajectories of the particles reaching the lung periphery, and particle deposition data and its significance to lung physiology.

2. A rhythmically expanding alveolus (Case A)

2.1. *Statement of the problem*

Suppose that a spherical cap of radius R is attached at its rim to a circular opening of radius a in an infinite plane. During the rhythmical process of expansion and contraction the half-conical angle η_0 (see figure 2) is held constant for all times. Since this maintains the configuration in a self-similar mode, the rate $\dot{R}$ at which the radius changes also governs the rate at which the plane expands laterally; explicitly, the radial velocity component of the plane is given by $\rho\dot{R}/R$. Here, ρ denotes the radial coordinate in the circular cylindrical system (ρ, ϕ, z), its origin being located at the centre of the rim. The flow dynamics are governed by the quasi-static Stokes equation,

$$\mu\nabla^2\boldsymbol{v} = \nabla p, \tag{1}$$

for incompressible fluids,

$$\nabla \cdot \boldsymbol{v} = 0. \tag{2}$$

Boundary conditions for a flow adhering to the moving boundaries of the cap and the plane are, respectively,

$$\begin{aligned}\boldsymbol{v}_{P/A} = \boldsymbol{v}_{P/O} + \boldsymbol{v}_{O/A} = \dot{R}\boldsymbol{i}_r + \dot{h}\boldsymbol{i}_z = \dot{R}\boldsymbol{i}_r + \dot{R}\cos\eta_0\boldsymbol{i}_z \\ = \dot{R}[\boldsymbol{i}_r(1 + \cos\theta\cos\eta_0) - \boldsymbol{i}_\theta\sin\theta\sin\eta_0]_{r=R},\end{aligned} \tag{3}$$

$$\boldsymbol{v}_{Q/A} = \dot{R}\frac{\rho}{R}\boldsymbol{i}_\rho, \tag{4}$$

where $\boldsymbol{v}_{P/A}$ denotes the relative velocity of a general point P lying on the sphere with respect to point A, the latter assumed to be at rest. The origin of the spherical coordinate system (r, θ, φ) is located at the centre of the spherical cap, with φ and θ representing the azimuthal and latitudinal angles, respectively. Here, $\boldsymbol{i}_r$ and $\boldsymbol{i}_\theta$ denote unit vectors in the indicated directions. The velocity, $\boldsymbol{v}_{Q/A}$, of a general point Q lying on the plane with respect to point A possesses only a radial component which grows linearly with respect to the distance of Q from A so as to maintain a uniform radial rate of strain in the alveolar tissue. Clearly, $\boldsymbol{v}_{P/A}$ and $\boldsymbol{v}_{Q/A}$ are identical at the rim. The flow field far from the cap and the plane is assumed to vanish.

2.2. *Method of solution*

Polar toroidal coordinates (ξ, η, ϕ) are well suited to the problem configuration. A description of this system is provided by Happel & Brenner (1983). We define

$$z = a\frac{\sin\eta}{\cosh\xi - \cos\eta}, \qquad \rho = a\frac{\sinh\xi}{\cosh\xi - \cos\eta} \quad (0 \leqslant \eta \leqslant 2\pi, \quad 0 \leqslant \xi < \infty), \tag{5}$$

where the spherical cap is given by $\eta = \eta_0 < \pi$. The axis of symmetry is given by $\xi = 0$, whereas the plane with the central circular hole corresponds to $\eta = 2\pi$.

Boundary conditions (3) and (4) are now rewritten to yield

$$\left.\begin{aligned} v_\eta &= -\dot{R}\sin^2\eta_0\frac{s}{s - t_0} \\ v_\xi &= -\dot{R}t_0\sin\eta_0\frac{\sinh\xi}{s - t_0} \end{aligned}\right\} \quad \text{at } \eta = \eta_0, \tag{6}$$

$$\left.\begin{aligned} v_\eta &= 0 \\ v_\xi &= -\dot{R}\sin\eta_0\frac{\sinh\xi}{s - 1} \end{aligned}\right\} \quad \text{at } \eta = 2\pi \tag{7}$$

where we used the abbreviated symbols

$$s = \cosh\xi, \quad t = \cos\eta, \quad t_0 = \cos\eta_0, \tag{8}$$

and where v_ξ and v_η are the velocity components in the ξ- and η-directions, respectively.

Since the problem is axisymmetric, a stream function $\tilde{\psi}$ can be defined satisfying the continuity equation (2) identically:

$$v_\xi = -\frac{(s - t)^2}{R^2\sin^2\eta_0\sinh\xi}\frac{\partial\tilde{\psi}}{\partial\eta}, \tag{9a}$$

$$v_\eta = \frac{(s - t)^2}{R^2\sin^2\eta_0\sinh\xi}\frac{\partial\tilde{\psi}}{\partial\xi}. \tag{9b}$$

Consequently, the Stokes equation (1) for $\tilde{\psi}$ is reduced to (Payne & Pell 1960)

$$\mathrm{L}_{-1}^2\tilde{\psi} = 0, \tag{9c}$$

where

$$\mathrm{L}_{-1} = \frac{\partial^2}{\partial\rho^2} - \frac{1}{\rho}\frac{\partial}{\partial\rho} + \frac{\partial^2}{\partial z^2}. \tag{9d}$$

Upon rewriting boundary conditions (6) and (7) in terms of the stream function, and integrating with respect to ξ, we obtain

$$[\psi]_{\eta=\eta_0} = \sin\eta_0 \left[\frac{1}{s-t_0} + \frac{t_0}{2(s-t_0)^2}\right] + \beta, \tag{10}$$

$$\left[\frac{\partial\psi}{\partial\eta}\right]_{\eta=\eta_0} = \frac{t_0 \sinh^2\xi}{(s-t_0)^3}, \tag{11}$$

$$[\psi]_{\eta=2\pi} = \beta, \tag{12}$$

$$\left[\frac{\partial\psi}{\partial\eta}\right]_{\eta=2\pi} = \frac{\sinh^2\xi}{(s-1)^3}, \tag{13}$$

where the non-dimensional stream function ψ is defined as

$$\psi = \tilde{\psi}/R^2\dot{R}\sin^3\eta_0. \tag{14}$$

Equation (14) is totally devoid of time-dependent terms. The constant of integration β was chosen such that

$$\beta = -\frac{(2-t_0)\sin\eta_0}{2(1-t_0)^2}, \tag{15}$$

so that ψ vanishes along the symmetry axis $\xi = 0$ ($s = 1$). Obviously, $\psi = \beta$ for $\xi \to \infty$ (the circular line at $z = 0$, $\rho = a$ defining the rim), whence β provides the non-dimensional volumetric flow rate at which fluid enters the spherical cap.

2.2.1. *Stream function representation*

Payne (1958) and later Payne & Pell (1960) point out that a useful stream-function representation in toroidal coordinates may depend crucially upon the specific boundary geometry involved. To quote them 'A combination suitable for one problem may be completely intractable for another'. Indeed the following solution representation seems to be appropriate to our specific problem:

$$\psi = \frac{\sinh^2\xi\sin\eta}{(s-t)^3} - \frac{\sin\eta_0(2-t_0)}{2(1-t_0)^2}\left[1-\left(\frac{1-t}{s-t}\right)^{3/2}\right] + \psi_h, \tag{16}$$

where ψ_h possesses a representation similar to one suggested by Payne & Pell (1960), and Vuong & Sadhal (1989). Explicitly,

$$\psi_h = (s-t)^{-3/2}\sinh^2\xi \int_0^\infty F_h(\alpha,\eta) P'_{-1/2+i\alpha}(s)\,d\alpha \tag{17}$$

where

$$F_h(\alpha,\eta) = \cos\eta\left[A(\alpha)\frac{\cosh[(2\pi-\eta)\alpha]}{\cosh[(2\pi-\eta_0)\alpha]} + B(\alpha)\frac{\sinh[(2\pi-\eta)\alpha]}{\sinh[(2\pi-\eta_0)\alpha]}\right]$$
$$-\sin\eta\left[C(\alpha)\frac{\cosh[(2\pi-\eta)\alpha]}{\cosh[(2\pi-\eta_0)\alpha]} + D(\alpha)\frac{\sinh[(2\pi-\eta)\alpha]}{\sinh[(2\pi-\eta_0)\alpha]}\right]. \tag{18}$$

Here, $A(\alpha)$, $B(\alpha)$, $C(\alpha)$ and $D(\alpha)$ are unknown functions of α to be determined by application of the boundary conditions. Clearly, the functions of α and η multiplying $A(\alpha)$, $B(\alpha)$ etc. are all less than or equal to unity, since the solution domain is confined to the region $\eta_0 < \eta < 2\pi$ where $\eta_0 < \pi$. The function $P'_{-1/2+i\alpha}(s)$ is the derivative with respect to s of the Legendre function of complex degree, $P_{-1/2+i\alpha}(s)$ (see Abramowitz

& Stegun 1965 and Zhurina & Karmazina 1966, the latter providing a comprehensive overview of this function and its derivatives).

The first term of (16) is the well-known solution for ideal-fluid stagnation flow, which can easily be shown to satisfy Stokes equations with no effect on the pressure field. It also exactly satisfies the boundary conditions on the stretching plane. The first term within the square brackets is simply a constant, representing the value of ψ at the corner which must be equal to the total volumetric flow through the expanding spherical cap β. The second term in square brackets represents the Stokes flow through a circular aperture (Happel & Brenner 1983) rewritten in toroidal coordinates.

It proves useful to establish an integral representation of the first term in (16) and the second term in the square brackets. Explicitly, we seek expressions for the functions F_{p1} and F_{p2}, appearing in the following integral equations:

$$\sinh^2\xi(s-t)^{-3/2}\int_0^\infty F_{p1}(\alpha,\eta)P'_{-1/2+\mathrm{i}\alpha}(s)\,\mathrm{d}\alpha=\frac{\sin\eta\sinh^2\xi}{(s-t)^3} \tag{19a}$$

and

$$\sinh^2\xi(s-t)^{-3/2}\int_0^\infty F_{p2}(\alpha,\eta)P'_{-1/2+\mathrm{i}\alpha}(s)\,\mathrm{d}\alpha=-\beta\left(\frac{1-t}{s-t}\right)^{3/2}. \tag{19b}$$

From (A 1) and (A 2) in the Appendix we obtain

$$F_{p1}(\alpha,\eta)=-2\sqrt{2}\sin\eta\frac{\cosh\left[(\eta-\pi)\alpha\right]}{\cosh(\pi\alpha)}, \tag{20a}$$

$$F_{p2}(\alpha,\eta)=\beta\frac{(1-t)^{3/2}\alpha}{\alpha^2+\frac{1}{4}}\tanh(\pi\alpha). \tag{20b}$$

Hence, another useful representation of ψ is

$$\psi=\beta+(s-t)^{-3/2}\sinh^2\xi\int_0^\infty[F_h(\alpha,\eta)+F_{p1}(\alpha,\eta)+F_{p2}(\alpha,\eta)]P'_{-1/2+\mathrm{i}\alpha}(s)\,\mathrm{d}\alpha. \tag{21}$$

Equations (16) and (21) will be used interchangeably.

2.2.2. *The solution for $A(\alpha)$, $B(\alpha)$, $C(\alpha)$ and $D(\alpha)$*

Upon introducing (16) into (12) we easily obtain

$$\psi_h(\alpha,2\pi)=0$$

or, from (17),

$$F_h(\alpha,2\pi)=0. \tag{22}$$

Substitution of (16) into (13) yields

$$\frac{\partial\psi_h}{\partial\eta}=0\quad\text{at }\eta=2\pi$$

or, from (22) and (17),

$$\frac{\partial F_h(\alpha,\eta)}{\partial\eta}=0\quad\text{at }\eta=2\pi. \tag{23}$$

Introduce (21) into (10) and utilize the inversion formulas provided in the Appendix to obtain, after some lengthy computations,

$$\begin{aligned}F_h(\alpha,\eta_0)&=\frac{4\sin\eta_0}{\sqrt{2}}\frac{\alpha^2}{\alpha^2+\frac{1}{4}}\frac{\cosh\left[(\eta_0-\pi)\alpha\right]}{\cosh(\pi\alpha)}+\frac{t_0}{\sqrt{2}}\frac{\alpha}{\alpha^2+\frac{1}{4}}\frac{\sinh\left[(\pi-\eta_0)\alpha\right]}{\cosh(\pi\alpha)}\\&\overset{\text{def}}{\equiv}E(\alpha,\eta_0).\end{aligned} \tag{24}$$

Similarly, upon substituting (21) into (11), and using (10) together with the inversion formulas in the Appendix, we obtain

$$\frac{\partial F_h}{\partial \eta}(\alpha,\eta_0) = -2\sqrt{2}\alpha \sin\eta_0 \frac{\sinh[(\eta_0-\pi)\alpha]}{\cosh(\pi\alpha)} - \frac{3}{\sqrt{2}}\sin\eta_0 \frac{\alpha}{\alpha^2+\frac{1}{4}}\frac{\sinh[(\eta_0-\pi)\alpha]}{\cosh(\pi\alpha)}$$
$$+\frac{3}{\sqrt{2}}\frac{t_0}{\sin\eta_0}\frac{\alpha}{\alpha^2+\frac{1}{4}}\frac{1}{\cosh(\pi\alpha)}$$
$$\times\{\alpha\sin\eta_0\cosh[(\eta_0-\pi)\alpha]+\cos\eta_0\sinh[(\eta_0-\pi)\alpha]\}$$
$$\stackrel{\text{def}}{\equiv} G(\alpha,\eta_0). \tag{25}$$

Introduction of (22), (23), (24) and (25) into (18) yields the following expressions for the unknown coefficients:

$$A(\alpha) = 0, \tag{26a}$$
$$B(\alpha) = -\frac{-G\sin\eta_0 + E\{\cos\eta_0 - \alpha\sin\eta_0\coth[(2\pi-\eta_0)\alpha]\}}{1-\alpha^2\sin^2\eta_0/\sinh^2[(2\pi-\eta_0)\alpha]}, \tag{26b}$$
$$C(\alpha) = -\alpha B\coth[(2\pi-\eta_0)\alpha] \tag{26c}$$

and

$$D(\alpha) = -\frac{E(1+\alpha^2)\sin\eta_0 + G\{\cos\eta_0 + \alpha\sin\eta_0\coth[(2\pi-\eta_0)\alpha]\}}{1-\alpha^2\sin^2\eta_0/\sinh^2[(2\pi-\eta_0)\alpha]}. \tag{26d}$$

Thus, for a given value of η_0, upon using (26*a–d*) together with the definitions of E and G in (24), (25) and (16)–(18), the stream function ψ can be calculated at any position (ξ,η).

2.3. *Results and discussion* (*Case A*)

Flow field considerations. It is important to validate convergence of the integral representation (16), especially to demonstrate that no infinite velocities exist in the solution domain. The functions E and G defined in (24) and (25) decay exponentially like $\exp(-\alpha\eta_0)$ and $\alpha\exp(-\alpha\eta_0)$ respectively, for large values of α, and algebraically like $O(\alpha^2)$ for small values of α. The behaviour of B, C and D defined in (26) is quite similar. For large values of α they decay like $\alpha^n\exp(-\alpha\eta_0)$ $(n>2)$, whereas for small values of α their decay is algebraic.

The Legendre polynomials are of order $\alpha^{1/2}$ for large values of α and possess a zero value for $\alpha = 0$. Hence, integration with respect to α poses no convergence problem over the entire domain of integration even for the worst case, when $\eta = \eta_0$. Practically, the integration can be carried out over a domain whose upper bound is given by any value of α that satisfies the inequality $\alpha^2 \ll \exp(\alpha\eta_0)$.

The solution for ψ_h converges even faster for values of η lying inside the domain $\eta_0 < \eta < 2\pi$ ($\eta = \eta_0$ being the worst case) as can easily be verified from (18).

Convergence of velocities in the vicinity of the spherical cap is easily verified. (Note that far from the cap the velocity grows linearly due to the self-similar boundary condition imposed on the flat surface). From (9) and the expression for ψ in (17), the velocity for large values of ξ can be determined from the fact that $P'_{-1/2+i\alpha}(s) = O(e^{-3/2\xi})$ whence $\psi_h = O(e^{-\xi})$. Therefore, the velocities at the cap rim ($\xi\to\infty$) possess a finite value (which could be zero if so required by the boundary conditions). On the other hand, for small values of ξ, $P'_{-1/2+i\alpha}(s) = O(1)$ and $\psi_h = O(\xi^2)$, whence the velocities are of order ξ, i.e. are finite in value (which could again be zero, if so required). Accordingly, the proposed solution converges everywhere within the

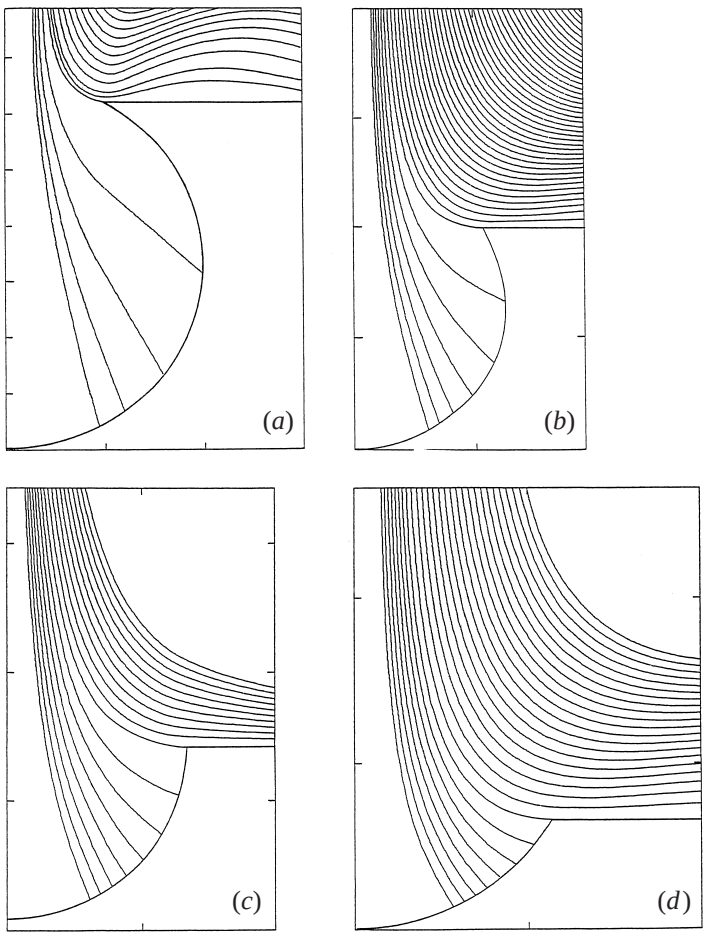

FIGURE 3. Streamline maps for half-conical angles (*a*) $\eta_0 = 30°$, (*b*) $\eta_0 = 60°$, (*c*) $\eta_0 = 90°$, (*d*) $\eta_0 = 120°$.

solution domain as a consequence of the addition of the first two explicit terms in (16).

The subsequent inversions used, namely (A 3)–(A 5), each possess a very slowly theoretically converging integral term (the one including $\tanh(\pi\alpha)$). However, the representation suggested in (16) eliminates all of these particular terms and facilitates the fast converging results for E and G (unlike those obtained by Vuong & Sadhal 1989, who still had to circumvent this difficulty in their analysis for two expanding vapour bubbles). Without the first term of (16) a solution could not practically be achieved. The second term of (16), which appears to possess no divergent properties of its own, is also required to speed up convergence.

In the vicinity of the hemispherical cap the velocity is always finite (figure 3). However, infinite velocities arise far from the cap owing to the infinite velocities specified at the far end of the plane. Figures 3(*a*) to 3(*d*) each depict streamlines obtained from (16)–(17) for various values of η_0. Each streamline represents a constant value of ψ, which is equally incremented in the streamline map. The results show that the flow rate near the symmetry axis is small compared with that in the rim region.

For small η_0, a sharp directional change of the streamline entering the corner occurs. Larger aerosol particles with some inertia may not be able to follow those sharp streamlines so that their deposition sites are likely to accumulate closer to the axis, whereas small inertialess particles which could move along the curved streamlines tend to deposit close to the rim (Haber & Tsuda 1998).

3. Alternating shear flow over an expanding alveolus

Steady shear flow over a plane wall that possesses a rigid cavity in the form of a spherical cap was studied by Pozrikidis (1994) employing a numerical boundary integral method. Based upon normal breathing frequencies, the Womersley numbers that prevail in the lung periphery are much smaller than unity. Consequently, the solution $\boldsymbol{v}^{shr}$ obtained by Pozrikidis (that is defined for unity depression radius R and unit shear rate) can be utilized to solve the quasi-steady problem for alternating shear rates $G(t)$ and combined with the time-dependent flow generated by the alveolus expansion $\dot{R}(t)\boldsymbol{v}^{exp}$, namely

$$\boldsymbol{v} = \dot{R}\boldsymbol{v}^{exp} + RG\boldsymbol{v}^{shr}. \tag{27}$$

The non-dimensional components of $\boldsymbol{v}^{exp}$ are derived from (9) and (14) for $\eta_0 = 90°$:

$$(v_\xi)^{exp} = -\frac{\sinh\xi(\cosh\xi\cos\eta - 2\sin^2\eta - 1)}{(\cosh\xi - \cos\eta)^2} - \tfrac{3}{2}\sin\eta\tanh(\xi/2)\left(\frac{1-\cos\eta}{\cosh\xi - \cos\eta}\right)^{1/2}$$
$$+\frac{3}{2}\frac{\sin\eta\sinh\xi}{(\cosh\xi - \cos\eta)^{1/2}}\int_0^\infty F(\alpha,\eta)P'_{-1/2+i\alpha}(\cosh\xi)\,d\alpha$$
$$-\sinh\xi(\cosh\xi - \cos\eta)^{1/2}\int\frac{\partial F(\alpha,\eta)}{\partial\eta}P'_{-1/2+i\alpha}(\cosh\xi)\,d\alpha, \tag{28a}$$

$$(v_\eta)^{exp} = \frac{\sin\eta(-\cosh^2\xi - 2\cos\eta\cosh\xi + 3)}{(\cosh\xi - \cos\eta)^2} - \frac{3}{2}\frac{(1-\cos\eta)^{3/2}}{(\cosh\xi - \cos\eta)^{1/2}}$$
$$+\frac{(\cosh^2\xi - 4\cosh\xi\cos\eta + 3)}{2(\cosh\xi - \cos\eta)^{1/2}}\int_0^\infty F(\alpha,\eta)P'_{-1/2+i\alpha}(\cosh\xi)\,d\alpha$$
$$+\sinh^2\xi(\cosh\xi - \cos\eta)^{1/2}\int F(\alpha,\eta)P''_{-1/2+i\alpha}(\cosh\xi)\,d\alpha \tag{28b}$$

where $\pi/2 < \eta < 2\pi$.

The time-periodic functions RG and $\dot{R}$ possess identical periodicities and almost similar shapes (Miki *et al.* 1993). The ratio of $\dot{R}$ to RG increases as we go deeper into the acinus, eventually approaching infinity at the acinar end. Streamlines for the combined velocity field $\boldsymbol{v}$, (27), can be obtained from the following non-dimensional expression:

$$\boldsymbol{v}' = \lambda\boldsymbol{v}^{exp} + \boldsymbol{v}^{shr}, \tag{29}$$

where $\lambda(t) = \dot{R}/RG$. (Notice that (29) is used instead of the actual combined velocity field (27) to emphasize that the streamline maps depend only upon the two non-dimensional parameters λ and η_0). Alternatively, in terms of the instantaneous volumetric flow Q_t inside an alveolated airway, the instantaneous volumetric flow entering the alveolus Q, the instantaneous radii R and R_t of the alveolus and the

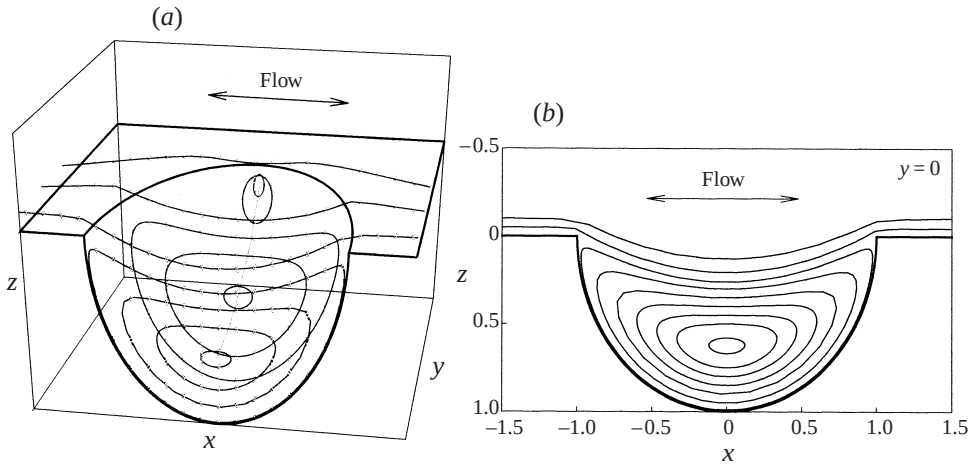

FIGURE 4. Streamline map for the shear flow over a hemispherical cavity (from Pozrikidis 1994). No expansion of alveolar walls is assumed ($\lambda_0 = 0$). (*a*) A three-dimensional view of the streamline map in the alveolar cavity; the dotted line, lying on the (y, z)-plane ($x = 0$), indicates a stagnation line which connects the 'centres' of recirculating eddies in the alveolar cavity. (*b*) A streamline map on the symmetry plane ($y = 0$).

airway, respectively

$$\lambda(t) = \frac{\dot{R}}{RG} \approx \frac{Q}{8Q_t}\frac{R_t^3}{R^3}. \tag{30}$$

3.1. *Results and Discussion* (*Cases A+B*)

It is important to distinguish between cases in which λ is fixed during breathing (the ductal and the alveolar flows are synchronized) or time dependent (a small asynchrony or phase lag exists). For fixed λ, (denoted λ_0) the streamline maps remain self-similar during the entire breathing period and scale with the alveolus radius. Thus, a single map for, say, $R = 1$ is sufficient to describe the flow streamlines. Figures 4 to 6 illustrate various streamline maps for different but time-independent (fixed) λ values.

Figure 4(a, b) depicts the case $\lambda = 0$ that corresponds to a rigid-wall alveolus. In this case, addressed by Pozrikidis (1994), a dividing surface exists that separates the outer flow field from the eddy existing inside the alveolus. Figure 4(a) shows a three-dimensional view of the streamline map, where the dotted line that lies on the (y, z)-plane indicates a stagnation line which connects the 'centres' of apparent recirculating eddies in the alveolar cavity. Figure 4(b) illustrates a two-dimensional view of the streamlines at the $y = 0$ plane. It clearly shows the dividing surface and the single stagnation point surrounded by closed streamlines. It should be noted that the stagnation line remains fixed in space during the entire breathing period.

For non-zero values of λ (figures 5 and 6), however, the whole streamline map topology is changed. For λ as small as 0.0025, the dividing surface observed in the case of $\lambda = 0$ vanishes and two instantaneous stagnation points are formed at the symmetry plane $y = 0$ (figure 5a). One point is found close to the alveolus centre ($x \approx -0.4R$) while the other is positioned very near to the proximal end of the alveolar opening ($x \approx -0.92R$). The first is surrounded by a closed rotating streamline, whereas the second is a saddle point, i.e. a singular point where a pair of streamlines move in, at the same time another pair of streamlines move away, and these streamlines are connected, forming a closed orbit on the (x, z) symmetry plane. A third pair of

streamlines connected with the saddle point, but not lying on the (x, z)-plane (see figure 6), is either directed toward the alveolus boundary when inhaling or inward (toward the saddle point) when exhaling. Note that the third pair of streamlines undergoes extremely rapid divergence (or convergence) (see thick black lines in the inset of figure 6) near the saddle point, suggesting a highly unstable flow field in the vicinity of the saddle point (see also thin black lines in the inset of figure 6). Both 'centre' and 'saddle points' on the symmetry plane are not fixed in space but move periodically during breathing as R varies periodically with time. A similar streamline map topology is observed for $\lambda = 0.005$ (figure 5*b*) where the two instantaneous stagnation points move closer together with increasing λ. The centre moves further away from the alveolus centreline and closer to the proximal end of the alveolar opening ($x \approx -0.54R$) and the saddle point moves slowly away from the proximal end ($x \approx -0.9R$). For higher values of λ, say $\lambda = 0.01$, 0.05 (figure 5*c*, *d*), the saddle point and the centre disappear altogether, and a streamline map similar to that of the expansion case prevails (e.g. figure 3). Consequently, for $0 < \lambda < 0.01$ two stagnation points exist inside the whole alveolar space (although their location is not fixed in space) whereas for $\lambda > 0.01$ no stagnation points exist (the value $\lambda = 0.01$ has only two digits of accuracy).

Streamline maps that were obtained by Tsuda *et al.* (1995*a*) for axisymmetric flow fields also depicted that under certain conditions saddle points were obtained near the proximal end of the alveolar opening; in that case they form a continuous concentric line of points.

In summary, we observe that within the alveolar cavity for non-zero λ, the symmetry plane is the only surface that may possess two instantaneous stagnation points, namely locations where all of the three velocity field components vanish. It also should be noted that in the present work saddle points exist only for the combined flows generated by the joint shear and the expansion motions of the alveolus during the breathing process.

When λ is time-dependent, one may expect all of the foregoing topologically different streamline maps to exist during a single breathing period. Indeed, it was inferred in Tsuda *et al.* (1999) based on surface-to-volume data of Miki *et al.* (1993) that the alveolar and ductal flows are normally asynchronized (roughly 10° magnitude) and as a result λ varies from zero to infinity during a single period. Thus, the slight movement of the saddle point during breathing can give rise to stochastic trajectories even in the quasi-static character of Stokes flow. This will briefly be illustrated in the next section.

4. A remark on stochastic trajectories of massless particles

Particle trajectories differ markedly from the streamline maps because trajectories follow the temporally evolving streamline map rather than one at some particular time. This is equivalent to the observation that the velocity field $\boldsymbol{v}$ is explicitly a function of time in computation of the trajectories.

4.1. *Particle trajectories*

Trajectories $\boldsymbol{r}_p(t)$ of massless particles are governed by the time-dependent equation (27), namely

$$\frac{\mathrm{d}\boldsymbol{r}_p}{\mathrm{d}t} = \dot{R}\boldsymbol{v}^{exp}(\boldsymbol{r}_p/R(t)) + RG\boldsymbol{v}^{shr}(\boldsymbol{r}_p/R(t)) \quad \text{and} \quad \boldsymbol{r}_p = \boldsymbol{r}_{p0} \quad \text{at } t = 0. \tag{31}$$

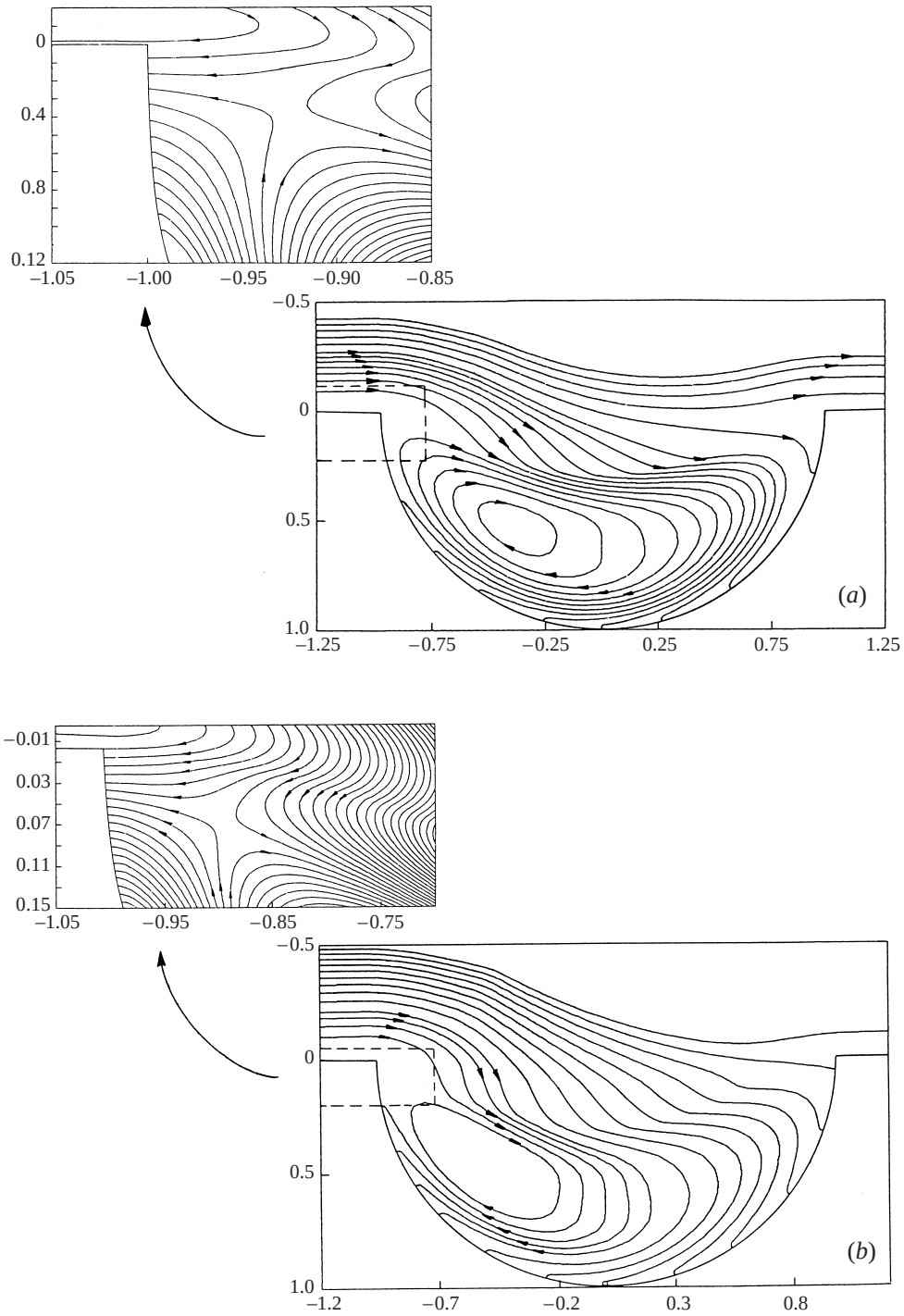

FIGURE 5. For caption see facing page.

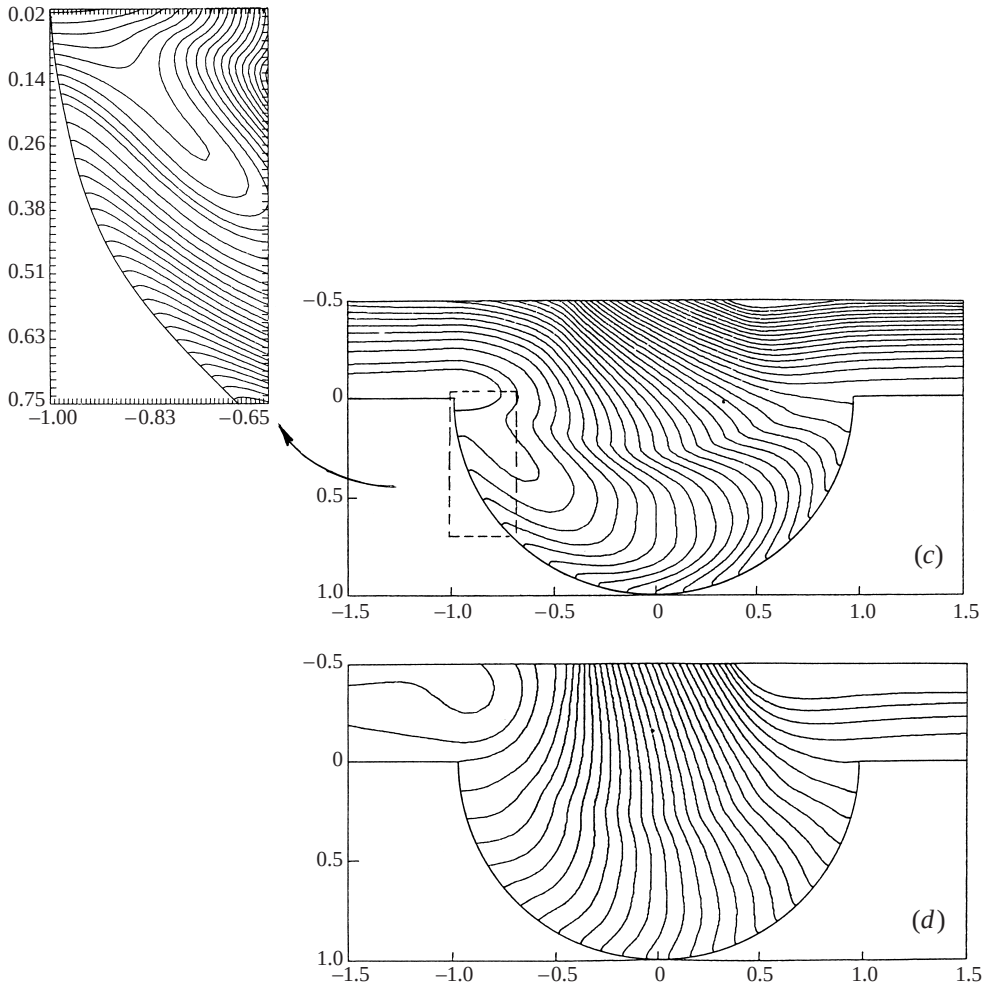

FIGURE 5. Streamline maps for the combined shear and expansion flows ($\lambda_0 \neq 0$). The flow field in the vicinity of a saddle point is depicted in the close-up figures: (*a*) $\lambda_0 = 0.0025$; (*b*) $\lambda_0 = 0.005$, (*c*) $\lambda_0 = 0.01$; (*d*) $\lambda_0 = 0.05$. In (a, b) two stagnation points are formed, in (c, d) no stagnation points are formed.

Note that since the quasi-steady velocity fields $\boldsymbol{v}^{exp}$ and $\boldsymbol{v}^{shr}$ were obtained for a unit radius hemisphere, particle location must be normalized with respect to the instantaneous radius of the alveolus $R(t)$. Physiologically, a small phase difference may exist between $\dot{R}$ and RG. It is common (albeit not exact) to assume that $R = R_0(1 + \kappa \cos(\omega t))$, $\dot{R} = -\omega R_0 \kappa \sin(\omega t)$ and $RG = -R_0 G_0 \sin(\omega t + \delta)$, where ω is the breathing frequency, R_0 is the mean radius of the alveolus, $R_0\kappa$ is the expansion amplitude of the alveolus, G_0 denotes the shear rate depending on the breathing volumetric flow and the alveolus location down the acinar tree, and δ stands for the phase angle. It is important to note that in this case the ratio $\lambda(t) = \dot{R}/RG = (\kappa\omega/G_0 \sin(\omega t)/\sin(\omega t + \delta)$ is not fixed during breathing due to the phase angle δ (a fact that will prove to be significant in the possible occurrence of stochastic pathlines).

Equation (31) can be slightly simplified by the following scaling of the radius vector

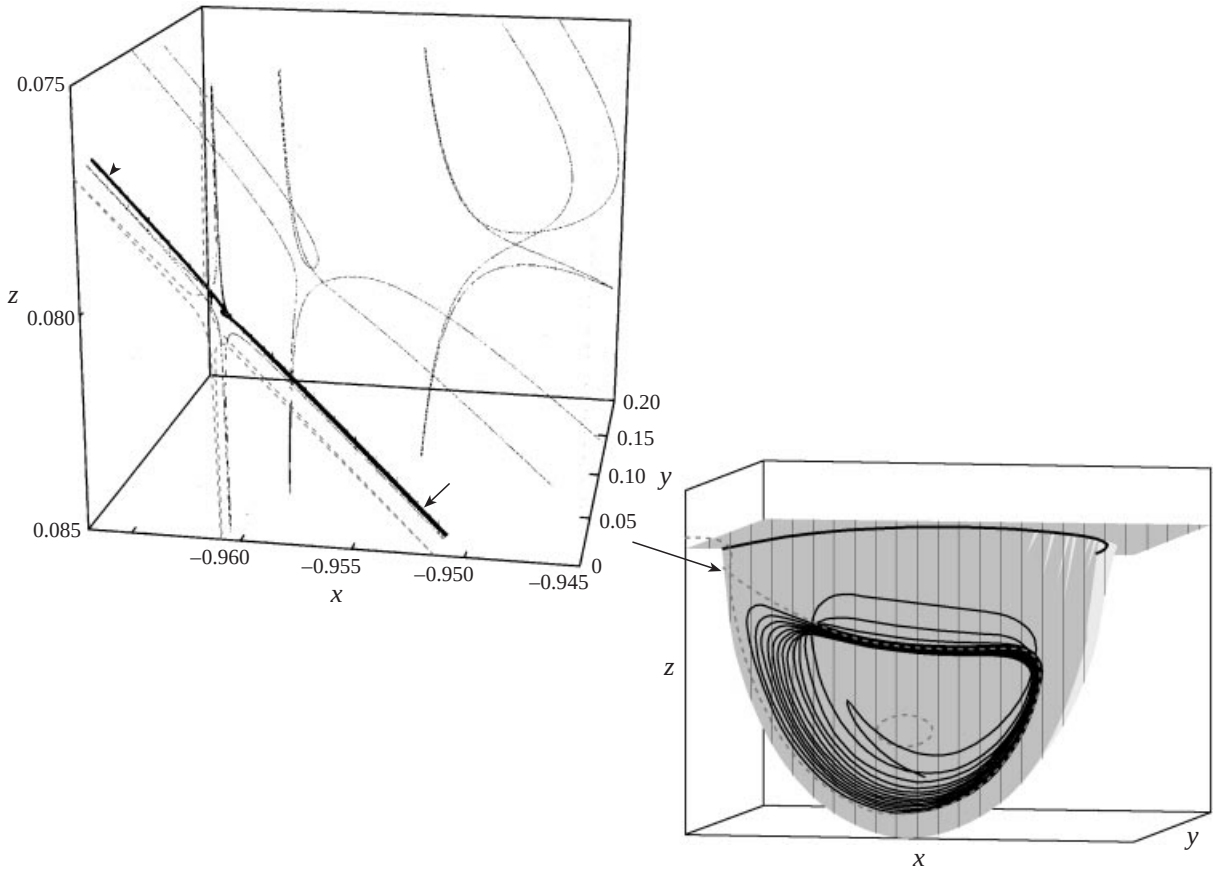

FIGURE 6. (*a*) A three-dimensional view of the streamline escaping from (or converging to) the stagnation points ('centre' and 'saddle point') on the symmetry plane, pointing outward toward the alveolus boundaries during inhaling, and inward toward stagnation during exhaling (shown as thick solid lines). Dashed lines show the streamlines on the symmetry plane associated with the stagnation points. $\lambda_0 = 0.0025$. (*b*) Details of streamline map in the vicinity of the saddle point. The streamlines escaping the saddle point undergo extremely rapid directional changes; one (arrow head) immediately ends on the alveolar walls near the proximal end of alveolar opening, the other (arrow) circles many times in the alveolar cavity (near the alveolar walls) before finally ending on the alveolar wall a far distance from the saddle point. The complex streamline structure near the saddle point is also shown (thin solid lines).

variable, and the time:

$$\hat{\boldsymbol{r}}_p = \boldsymbol{r}_p/R(t), \qquad \tau = \ln(R(t)/R_0) \tag{32}$$

to yield

$$\frac{\mathrm{d}\hat{\boldsymbol{r}}_p}{\mathrm{d}\tau} = \boldsymbol{v}^{exp}(\hat{\boldsymbol{r}}_p) + \boldsymbol{v}^{shr}(\hat{\boldsymbol{r}}_p)/\lambda(\tau) - \hat{\boldsymbol{r}}_p. \tag{33}$$

In what follows, we will treat the case where $\kappa = 0.1$, $\omega/G_0 = 0.025$ and $\delta = 2^\circ$, 10°, corresponding to the proximal region of the acinus, and describe trajectories on and off the symmetry planes.

Particles on the symmetry plane A particle initially located on the symmetry plane, $y_p\ (t = 0) = 0$, remains there and does not mix with particles outside the symmetry plane (and vice versa) since the velocity component in the y-direction $\mathrm{d}y_p/\mathrm{d}t$ on that plane vanish for all times. Their trajectories in the $(\hat{x}_p, \hat{z}_p)$ plane are governed by the following equations:†

$$\left.\begin{aligned} \frac{\mathrm{d}\hat{x}_p}{\mathrm{d}\tau} &= v_x^{exp}(\hat{x}_p, \hat{z}_p) + v_x^{shr}(\hat{x}_p, \hat{z}_p)/\lambda(\tau) - \hat{x}_p, \\ \frac{\mathrm{d}\hat{z}_p}{\mathrm{d}\tau} &= v_z^{exp}(\hat{x}_p, \hat{z}_p) + v_z^{shr}(\hat{x}_p, \hat{z}_p)/\lambda(\tau) - \hat{z}_p. \end{aligned}\right\} \tag{34}$$

This two-dimensional system is not autonomous, since τ appears explicitly, and therefore permits the appearance of stochastic trajectories (Wiggins 1990).

A fourth-order Runge–Kutta method was employed to solve numerically a non-dimensionalized equation (31) where R_0 was used to scale lengths, $1/\omega$ to scale time and $R_0\omega$ to scale velocities. Convergence was achieved for a time step value of 0.001. The velocity field components were calculated only once at approximately 10^4 evenly spaced locations inside the alveolus. Linear interpolation was used to calculate velocity components for in-between locations. Figure 7(*a*) illustrates a Poincaré map of a single particle placed initially at $x_{p0} = -0.35$, $z_{p0} = 0.5$ for the $\delta = 2^\circ$ case. Particle location was sampled after every period (2π) for 1000 periods. Evidently, a clear outline of a quasi-periodic torus is obtained which also validates the numerical scheme accuracy. It must be noted that a Poincaré map of the same particle trajectory for the $\delta = 0$ case appears as a single point revisited after every breathing cycle in accordance with the following proof (that was yet another measure that we applied to verify the accuracy of the numerical scheme). Note that, if $\delta = 0$, the ratio $\lambda(t)$ becomes time independent and equation (34) is an autonomous two-dimensional set of equations and hence integrable (Whittaker 1937). Thus, at the transformed $(\hat{x}_p, \hat{z}_p)$-plane, particle trajectories are determined by a function of $\hat{z}_p, \hat{x}_p$ and a free constant of integration. Hence, from equation (32), in the real (x_p, z_p)-plane, massless particle trajectories would exhibit periodic behaviour, sampling the same position after every breathing period $2\pi/\omega$. A Poincaré map for the whole symmetry plane is illustrated in figure 7(*b*) for the $\delta = 2^\circ$ case. Regions of stochasticity seem to appear bounded

† Symmetry of $\boldsymbol{v}^{exp}$ and $\boldsymbol{v}^{shr}$ with respect to the $y = 0$ plane implies that $\partial v_y/\partial y = 0$ at $y = 0$. Consequently, the continuity equation possesses the form $\partial v_x/\partial\hat{x} + \partial v_z/\partial\hat{z} = 0$ at $y = 0$. However, since $\partial v_x/\partial x + \partial v_z/\partial z = (\partial v_x/\partial\hat{x} + \partial v_z/\partial\hat{z})/R = 0$ a stream function ψ can be defined in the real (x_p, z_p)-plane. Thus, for the symmetry plane, equation (31) can in principle be rewritten as follows:

$$\frac{\mathrm{d}x_p}{\mathrm{d}t} = \frac{\partial\psi(x_p, z_p, t)}{\partial z_p}, \qquad \frac{\mathrm{d}z_p}{\mathrm{d}t} = -\frac{\partial\psi(x_p, z_p, t)}{\partial x_p}. \tag{35}$$

Obviously, equation (35) is a Hamiltonian, volume (area)-conserving dynamical system, a fact that also proved useful in checking the accuracy of the numerical scheme.

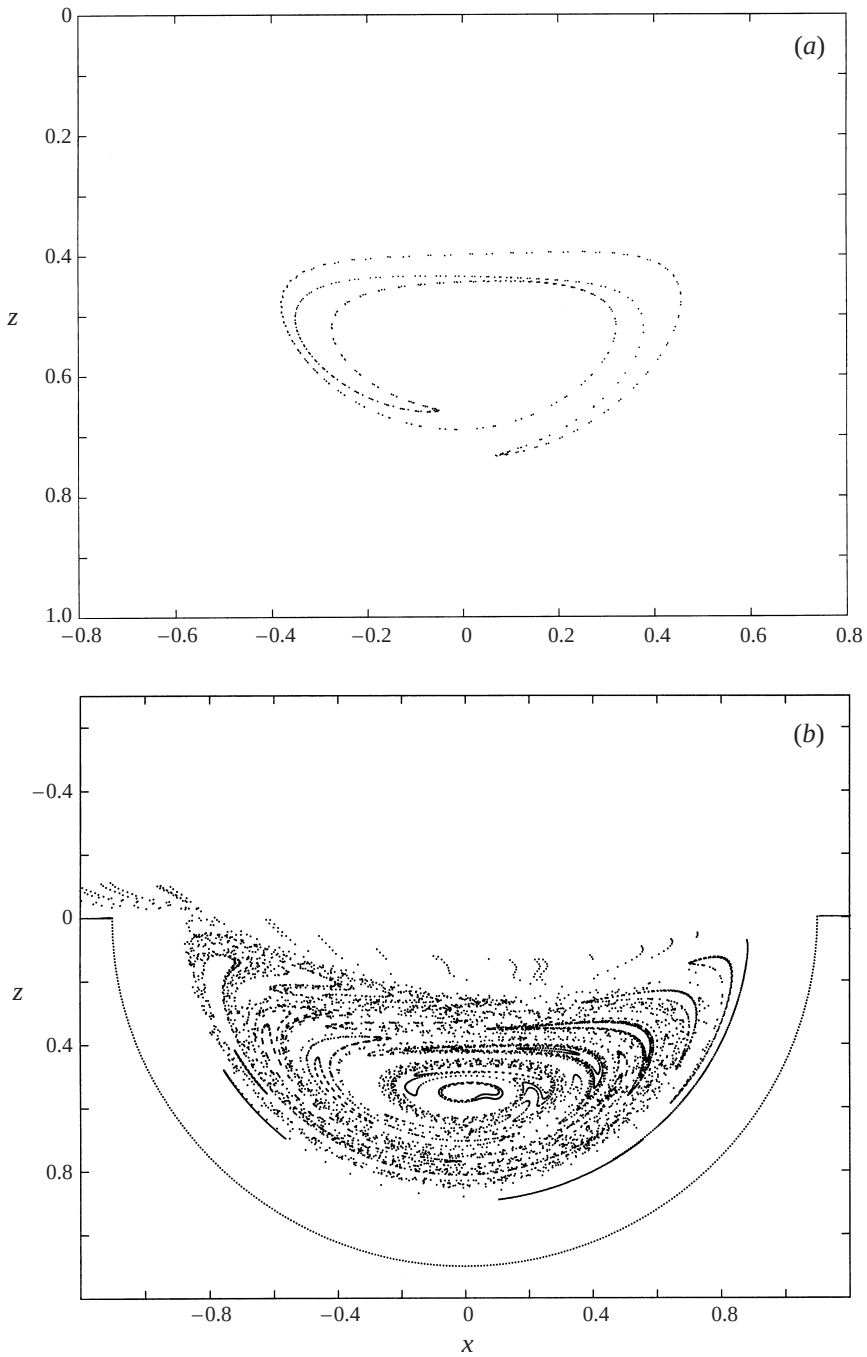

FIGURE 7. For caption see facing page.

by quasi-periodic surfaces. It is important to note that the observed stochastisity is part of the intrinsic dynamics of the system, and not due to an unpredictable random influence such as particle diffusion. Thus, the assertion that stochastic trajectories may exist for zero Reynolds numbers is here validated.

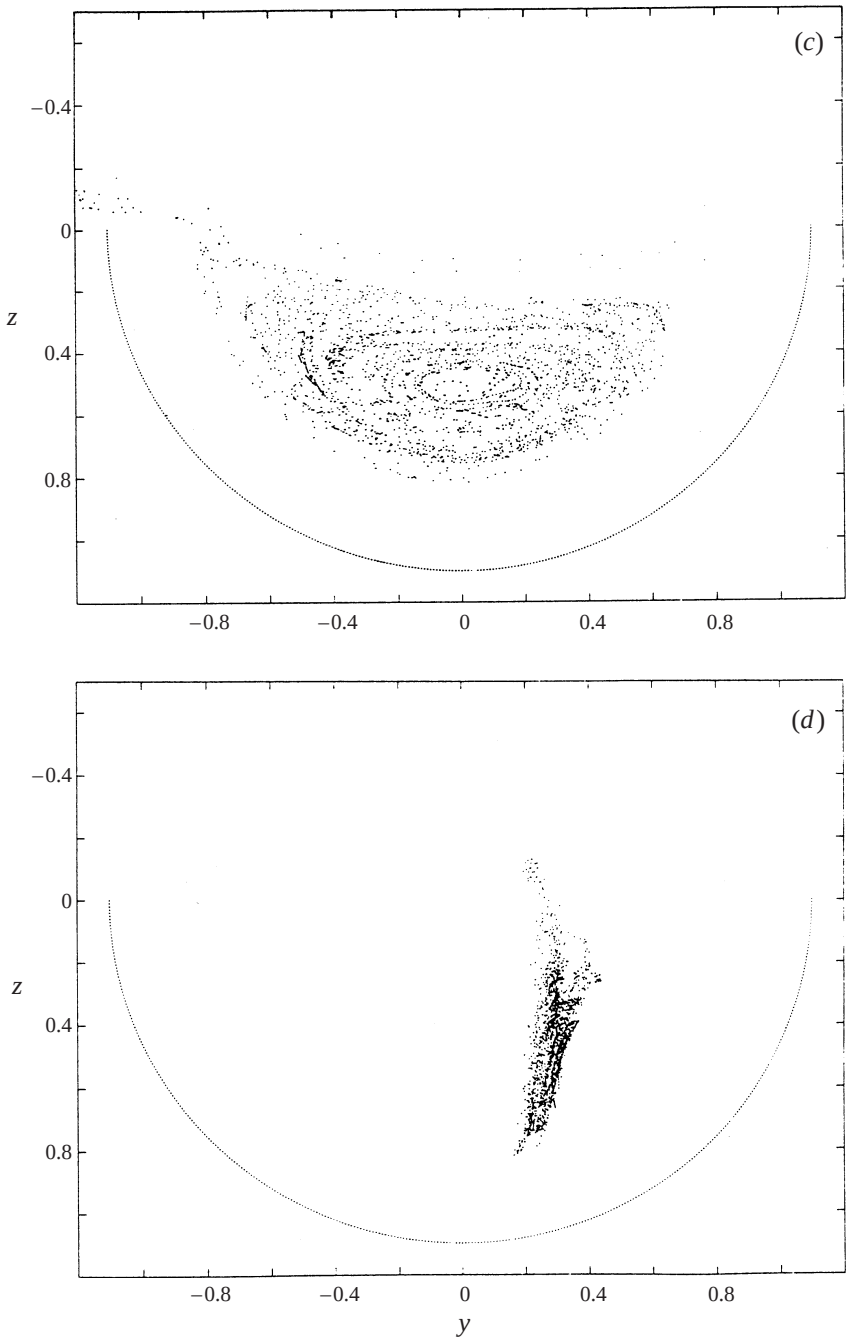

FIGURE 7. (*a*) A Poincaré map of a single particle placed initially at $x_{p0} = -0.35$, $z_{p0} = 0.5$. Particle location was sampled after every period (2π) for 1000 periods. A clear outline of a quasi-periodic torus is obtained. (*b*) A Poincaré map for points initially placed on the symmetry plane. All particle locations were sampled after every period (2π) for 500 periods. Regions of stochasticity seem to appear bounded by quasi-periodic surfaces. (*c*) and (*d*) A Poincaré map for points initially placed at $y = -0.3$. All particle locations were sampled after every period (2π) for 500 periods. Regions of stochasticity seem to appear bounded by quasi-periodic surfaces. In cases (*a*) and (*b*) $\lambda_0 = 0.0025$ and $\delta = 2^\circ$. In cases (*c*) and (*d*), $\lambda_0 = 0.0025$ and $\delta = 10^\circ$.

This may also resolve the open question raised by Tsuda *et al.* (1995*a*) of whether their findings of stochastic trajectories stem solely from non-zero Reynolds-number effects or it is an inherent property of the flow existing for zero-Reynolds-number flows as well.

Particles off the symmetry plane A particle initially positioned off the symmetry plane would generally outline a three-dimensional rotating pathline inside the alveolar space, but never cross the symmetry plane. The governing equations are given by (31), and due to the fact that the shear and expansion velocity fields satisfy the continuity equation the dynamical system is volume conserving. In the case $\delta = 0$, the flow is periodic owing to the reversibility property of Stokes' flows. Thus a Poincaré map of a trajectory appears as a single point revisited. Figure 7(*c*) illustrates a Poincaré map of particles initially located at $y = -0.3$ and $\delta = 10^\circ$. A careful examination of the Poincaré map reveals islands of quasi-periodic orbits even for small values of the phase angle. It is interesting to note that the points do not stay on the $y = -0.3$ plane and occupy a three-dimensional space (unlike the axisymmetric case dealt with by Tsuda *et al.* (1995*a*) where points remain confined to their azymuthal plane). Almost all points near the streamline that extends from the centre at the $y = 0$ plane remain in a nicely bounded volume and do not move far into neighbouring spaces inside the alveolar cavity. This was also validated in the next section where the extent of mixing inside the cavity is briefly addressed.

4.2. *A note on the extent of mixing in the alveolar cavity*

According to Ottino (1989) mixing is directly related to the rate of strain and vorticity that exist inside the flow. In this paper, we limit our analysis to the relative magnitude of mixing at various points inside the alveolus. First, one must exclude any periodic flows since their contribution to mixing is null. Thus, for synchronized alveolar and acinar flows where $\delta = 0$ no mixing can be expected. Second, if, however, as indeed observed, the acinar and alveolar flows are asynchronized we may expect mixing to occur.

The extent of mixing can be scaled if we consider the strain tensor based on the Poincaré mapping. In other words, instead of calculating the rate of strain based on the velocity field we calculate the relative displacement that adjacent particles undergo after a complete breathing cycle. We used four adjacent points forming a corner of a cubic test-cell whose sides are parallel to the (x, y, z) coordinate system. The points are $\mathrm{d}\boldsymbol{x}^{(i)}$ apart ($i = 1, 2, 3$) and are released. Their new position after a single period is monitored. Their relative displacement $\mathrm{d}\boldsymbol{u}^{(i)} = \mathrm{d}\boldsymbol{x}^{(i)}\ (t = 2\pi) - \mathrm{d}\boldsymbol{x}^{(i)}(t = 0)$ is then computed and the modified 'velocity gradient' $\boldsymbol{\epsilon}$ tensor (per unit time of a single period) can be derived from the following equation:

$$\mathrm{d}\boldsymbol{u}^{(i)} = \mathrm{d}\boldsymbol{x}^{(i)} \cdot \boldsymbol{\epsilon}. \tag{36}$$

Equation (36) provides three equations for every i for the nine unknown components of $\boldsymbol{\epsilon}$. Thus, $\boldsymbol{\epsilon}$ can easily be obtained from

$$\boldsymbol{\epsilon} = \{\mathrm{d}\boldsymbol{x}^{(1)}, \mathrm{d}\boldsymbol{x}^{(2)}, \mathrm{d}\boldsymbol{x}^{(3)}\}^{-1}\{\mathrm{d}\boldsymbol{u}^{(1)}, \mathrm{d}\boldsymbol{u}^{(2)}, \mathrm{d}\boldsymbol{u}^{(3)}\}. \tag{37}$$

The resulting 'strain' tensor $\boldsymbol{D}$ and 'rotation' tensor $\boldsymbol{\Omega}$ are

$$\boldsymbol{D} = 0.5(\boldsymbol{\epsilon} + \boldsymbol{\epsilon}^T), \qquad \boldsymbol{\Omega} = 0.5(\boldsymbol{\epsilon} - \boldsymbol{\epsilon}^T). \tag{38}$$

The 'stretching' at every point is proportional to the invariant $(\boldsymbol{D} : \boldsymbol{D})^{1/2}$ easily computed from the eigen values of $\boldsymbol{D}$. Application of the above definition of the strain

eliminates any contribution to $\boldsymbol{D}$ or $\boldsymbol{\Omega}$ stemming from periodic flows and we suggest using it as a simple measure by which the relative extent of mixing at different points inside the alveolus can be evaluated.

Figure 8 depicts the extent of stretching $(\boldsymbol{D}:\boldsymbol{D})^{1/2}$ and rotation $(\boldsymbol{\Omega}:\boldsymbol{\Omega})^{1/2}$ that a small cubic test cell (of side 0.0204) undergoes after a single breathing cycle for various positions of the test cell inside the alveolus. Careful examination of stretching and rotation on the symmetry plane (figure 8*a*) reveals that, for certain regions inside the alveolus, the extent of mixing is sensitive to the test-cell initial position. Regions of highest sensitivity are found near the closed streamline that originates from and returns to the saddle point at the symmetry plane and the area near the saddle point (see figure 5*a*). That fact confirms that stochastic behaviour of a particle placed initially in these regions is to be expected. Moreover, distinct regions of high and low values of stretching and rotation can be observed. High values exist invariably near the above-mentioned closed streamline and the saddle point. Thus, high stochasticity results in high values of mixing near the alveolus boundaries and close to the proximal end of the alveolar opening (negative x-values). Stretching can reach four times the value that exists in the undisturbed shear flow (normalized with respect to ω, the stretching value in the undisturbed shear flow is $G_0/2\omega = 20$).

Similar results are obtained off the symmetry plane (see figure 8*b*) where high stretching and rotation values exist near the alveolus boundaries, where the streamlines originating from the saddle point pass (see figure 6). Stretching and rotation values off the symmetry plane (figure 8*b*) are comparable to those at the symmetry plane (figure 8*a*). Moreover, in some places near the space adjacent to the saddle point on the off-symmetry plane stretching and rotation are even higher than at the symmetry plane $y = 0$ itself. This may be due to the contribution of the additional component of the velocity gradient in the y-direction (see figure 6). Smaller stretching and rotation values are observed in the region near the streamline that escapes the 'centre' towards the boundaries of the alveolus. This is also in good agreement with our previous conclusions deduced from the streamline maps.

4.3. *Physiological considerations*

Deposition of inhaled particles in the pulmonary acinus often has physiological and pathophysiological consequences. In this context, it is crucial to understand how aerosol particles are transported within the acinus and mix with residual alveolar gas because deposition is strongly influenced by mixing.

Several experimental studies show the complexity of aerosol mixing processes in the acinus. Davies (1972) argued that generally little mixing occurs between inhaled particles and residual alveolar gas, and any mixing that occurs in the acinar region should be solely due to the particles' own motion (Brownian motion, gravitational sedimentation, inertial streamline crossing), since no convective (flow-induced) mixing is expected at the acinar level. In aerosol bolus dispersion studies, on the other hand, Heyder and coworkers (Heyder *et al.* 1988; Anderson *et al.* 1989; Schulz *et al.* 1992) consistently observed that the deeper the bolus penetrated into the acinus, the more it became dispersed. They concluded that the observed mixing cannot be accounted for solely by the intrinsic motion of particles, and thus it should be attributable to flow-induced mixing. These findings strongly suggest that the deposition and mixing of aerosol particles are largely influenced by convection even at the level of the lung periphery. Our recent flow visualization studies performed in excised rat and rabbit lungs revealed extremely complex 'stretched and folded' fluid mixing patterns (Tsuda

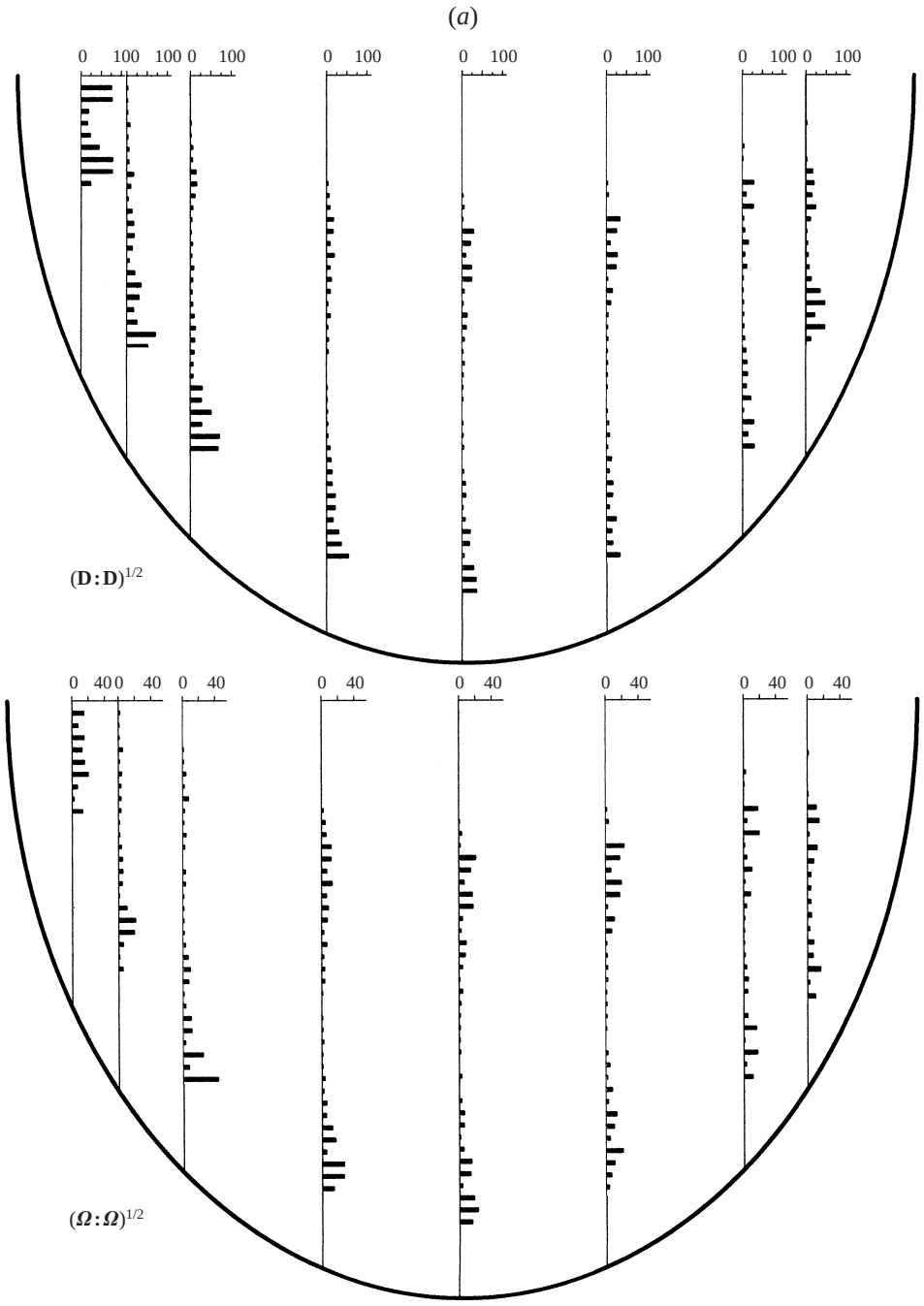

FIGURE 8. For caption see facing page.

et al. 1995*b*; Butler & Tsuda 1997), confirming the importance of convective mixing and suggesting the new possibility of a chaotic origin of mixing.

From the theoretical point of view, aerosol kinetics in the acinus have been considered as follows. A viscous flow is kinematically reversible if the wall motion of the conduit is reversible (Watson 1974; Taylor 1967). This leads to the notion that

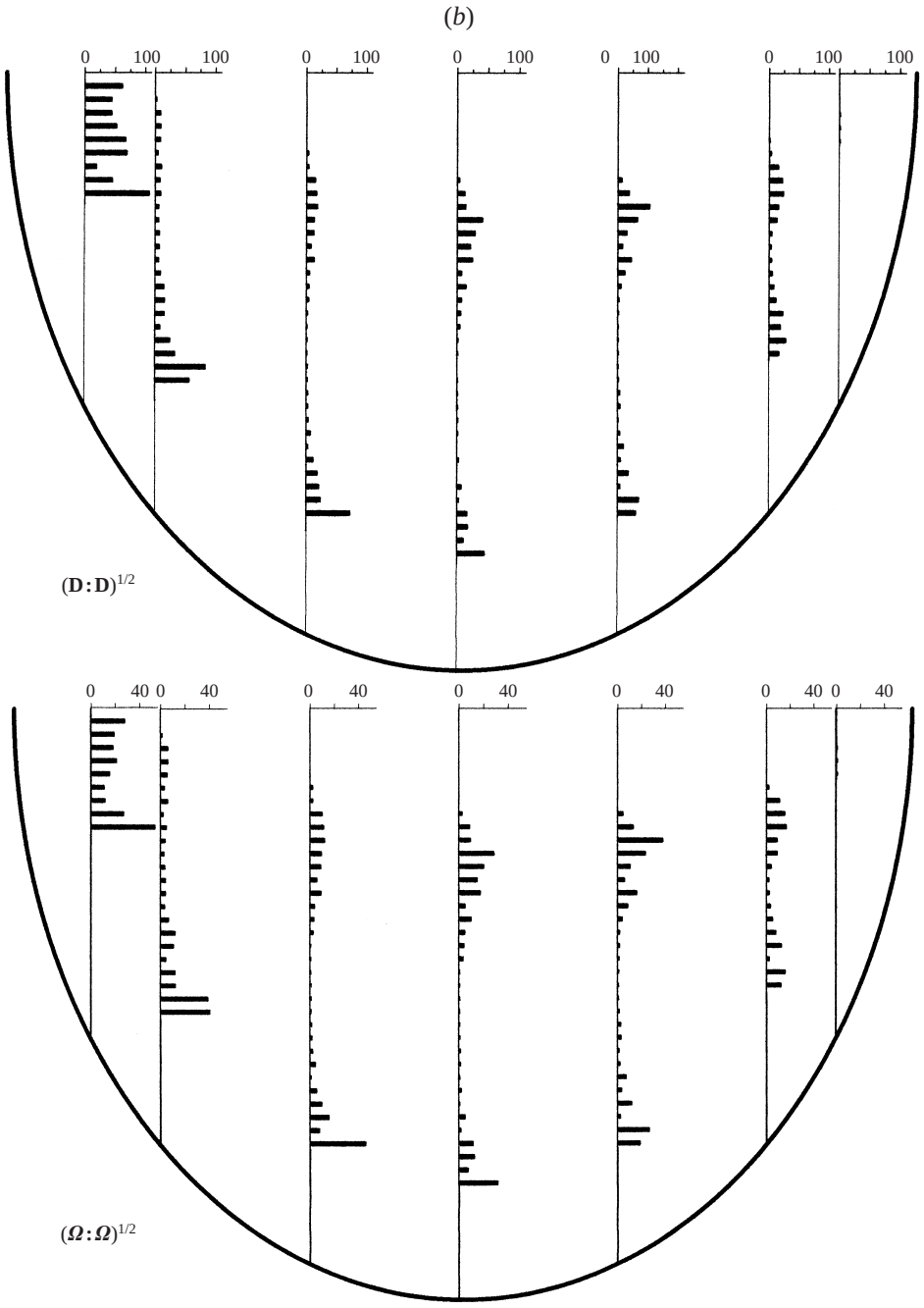

FIGURE 8. (*a*) A stretching and rotation map for points initially placed at $y = 0$. Here $\kappa = 0.1$, $\lambda_0 = 0.0025$ and $\delta = 10°$. Regions of stochasticity seem to appear near the closed streamline that extends from and returns to the saddle point. Strong mixing is obtained near the alveolus boundaries close to the proximal end of the alveolar opening. Low values are obtained near the centre and far from the proximal end. (*b*) A stretching and rotation map for points initially placed at $y = 0.408$, $\lambda_0 = 0.0025$ and $\delta = 10°$. Strong mixing is obtained near the alveolus boundaries close to the proximal end of the alveolar opening. Poor mixing is obtained near the streamline escaping the centre towards the alveolus boundary.

acinar flow should be reversible since it is viscous flow (the Reynolds number is much smaller than unity), and acinar walls expand and contract basically in a geometrically similar reversible fashion (Gil & Weibel 1972; Ardila *et al.* 1974; Gil *et al.* 1979; Weibel 1986; Miki *et al.* 1993). This line of thought, therefore, theoretically excludes the possibility of convective (flow-induced) mixing in the acinar region, contrary to the experimental results mentioned above. What are the possible mechanisms to explain mixing observed in the acinus?

Our current theoretical investigations addressing this question mainly focus on the effects of structural alveolation and cyclic wall motion on aerosol kinetics (Tsuda *et al.* 1994*a*, *b*; 1995*a*, 1999; and Butler & Tsuda 1997). In particular, studying the influence of time-dependent geometric expansion of the alveolar walls on flow behaviour, we have recently discovered that acinar flow can possibly be irreversible despite, its viscous nature (Tsuda *et al.* 1995*a*). In axisymmetric alveolated duct models which rhythmically expand and contract in a geometric similar manner, we found that the low-Reynolds-number viscous flow could be complex with a stagnation saddle point near the alveolar opening, and fluid particle pathlines derived therefrom become highly complex, irreversible, and unpredictable due to the high sensitivity to initial conditions, exhibiting phenomena characteristic of chaotic flow (Tsuda *et al.* 1995*a*). In the present study, a Stokes flow in a three-dimensional rhythmically expanding spherical alveolus with small flow asynchrony also exhibited very similar complex flow phenomena with essentially the same flow structure as in our previous axisymmetric model. These two studies, therefore, suggest that viscous acinar flow can exhibit chaotic behaviour, and thus induce convective mixing if there is a small perturbation on viscous flow conditions (e.g. small but non-zero Reynolds-number effects) or on reversible wall motion (e.g. small but non-zero wall hysteresis, asynchrony between ductal and alveolar entering flows, cardiac motion). Furthermore, the important geometric features of an acinar airway can be represented as a central convective channel surrounded by dead-end air pockets.

In summary, we have developed an analytical model of acinar fluid mechanics in a rhythmically expanding spherical alveolus and its vicinity to elucidate the basic physics operating on inhaled particles in the lung periphery. Results of this study together with our previous studies indicate that there is an unexpected level of complexity of aerosol mixing due to the unique geometric features (structural alveolation and rhythmic expansion), and suggest that radically new mechanisms of mixing, such as chaotic mixing, operate in the acinar region.

This research was supported by the Fund for The Promotion of Research at The Technion (SH), National Heart, Lung and Blood Institute Grant NIH HL-47428 (AT) and NIH HL-33009, HL-54885 (SH+JPB+AT), The Center for Absorption in Science, Ministry of Immigrant Absorption State of Israel (I.E) as well as by the Office of Basic Energy Sciences of the Department of Energy (HB). We are indebted to Professor Pozrikidis for providing us with his data on shear flow over a spherical cavity.

Appendix

The following Mehler–Fock integral inversions, fully described by Sneddon (1972) and conveniently summarized in the Appendix of Davis (1982), were required to

obtain (24) and (25). MacRobert (1948) has shown that

$$\frac{1}{(s-t)^{1/2}} = \sqrt{2}\int_0^\infty \frac{\cosh\left[(\eta-\pi)\alpha\right]}{\cosh(\pi\alpha)} P_{-1/2+i\alpha}(s)\,d\alpha \quad (0<\eta<2\pi). \tag{A 1}$$

Differentiation of (A 1) with respect to s yields

$$\frac{1}{(s-t)^{3/2}} = -2\sqrt{2}\int_0^\infty \frac{\cosh\left[(\eta-\pi)\alpha\right]}{\cosh(\pi\alpha)} P'_{-1/2+i\alpha}(s)\,d\alpha. \tag{A 2}$$

From the Appendices of Schneider, O'Neill & Brenner (1973) and Vuong & Sadhal (1989) (with minor modifications) for the region $0<\eta<2\pi$, we obtain

$$\frac{(s-t)^{1/2}}{\sinh^2\xi} = -\int_0^\infty \frac{1}{\alpha^2+\frac{1}{4}}\left[\alpha\tanh(\pi\alpha)(1-\cos\eta)^{1/2} + \frac{1}{\sqrt{2}}\frac{\cosh\left[(\eta-\pi)\alpha\right]}{\cosh(\pi\alpha)}\right] \times P'_{-1/2+i\alpha}(s)\,d\alpha, \tag{A 3}$$

$$\frac{1}{\sinh^2\xi(s-t)^{1/2}} = \int_0^\infty \frac{\alpha}{\alpha^2+\frac{1}{4}}\left[\frac{\sqrt{2}\sinh\left[(\pi-\eta)\alpha\right]}{\sin\eta\cosh(\pi\alpha)} - \frac{\tanh(\pi\alpha)}{(1-\cos\eta)^{1/2}}\right] P'_{-1/2+i\alpha}(s)\,d\alpha, \tag{A 4}$$

$$\frac{1}{\sinh^2\xi(s-t)^{1/2}} = \int_0^\infty \frac{\alpha}{\alpha^2+\frac{1}{4}}\left[\frac{2\sqrt{2}}{\sin^3\eta\cosh(\pi\alpha)}\{\alpha\sin\eta\cosh\left[(\eta-\pi)\alpha\right] + \cos\eta\sinh\left[(\pi-\eta)\alpha\right]\} - \frac{\tanh(\pi\alpha)}{(1-\cos\eta)^{3/2}}\right] P'_{-1/2+i\alpha}(s)\,d\alpha. \tag{A 5}$$

REFERENCES

Abramowitz, M. & Stegun, I. A. 1965 *Handbook of Mathematical Functions*. Dover.

Anderson, P. J., Blanchard, J. D., Brain, J. D., Feldman, H. A., McNamara, J. J. & Heyder, J. 1989 Effect of cystic fibrosis on inhaled aerosol boluses. *Am. Rev. Respir. Dis.* **140**, 1317–1324.

Ardila, R., Horie, T. & Hildebrandt, J. 1974 Macroscopic isotropy of lung expansion. *Respir. Physiol.* **20**, 105–115.

Avedisian, C. T. & Andres, R. P. 1978 Bubble nucleation in superheated liquid-liquid emulsions. *J. Colloid Interface Sci.* **64**, 438–453.

Brain, J. J., Blanchard, D. & Sweeney, T. D. 1989 Deposition and fate of inhaled pharmacologic aerosols. In *Provocative Challenge Procedures: Background and Methodology* (ed. S. D. Spector), pp. 1–36. Mount Kisco, NY: Futura.

Butler, J. P. & Tsuda, A. 1997 Effect of convective stretching and folding on aerosol mixing deep in the lung, assessed by approximate entropy. *J. Appl. Physiol.* **83**, 800–809.

Darquenne, C. & Paiva, M. 1996 Two- and three-dimensional simulations of aerosol transport and deposition in alveolar zone of human lung. *J. Appl. Physiol.* **80**, 1401–1414.

Davidson, M. R. & Fitz-Gerald, J. M. 1972 Flow patterns in models of small airway units of the lung. *J. Fluid Mech.* **52**, 161–177.

Davies, C. N. 1972 Breathing of half-micron aerosols: II Interpretation of experimental results. *J. Appl. Physiol.* **35**, 605–611.

Davis, A. M. J. 1982 Two phase Stokes flows distorted by a sphere straddling the interface. *Intl J. Multiphase Flow* **8**, 361–369.

El-Kareh & Secomb, T. W. 1996 Stokes flow impinging on a spherical cap on a plane wall. *Q. J. Mech. Appl. Maths* **49**, 179–193.

Gil, J., Bachofen, H., Gehr, P. & Weibel, E. R. 1979 Alveolar volume-surface area relation in air- and saline-filled lungs fixed by vascular perfusion. *J. Appl. Physiol.* **45**(5), 990–1001.

Gil, J. & Weibel, E. R. 1972 Morphological study of pressure-volume hysteresis in rat lungs fixed by vascular perfusion. *Respiratory Physiol.* **15**, 190–213.

Haber, S. & Tsuda, A. 1998 The effect of flow generated by a rhythmically expanding pulmonary acinus on aerosol dynamics. *J. Aerosol Sci.* **29**, 309–322.

Haefeli-Bleuer, B. & Weibel, E. R. 1988 Morphometry of the human pulmonary acinus. *Anat. Rec.* **220**, 401–414.

Happel, J. & Brenner, H. 1983 *Low Reynolds Number Hydrodynamics*. Kluwer.

Heyder, J., Blanchard, D., Feldman, H. A. & Brain, J. D. 1988 Convective mixing in human respiratory tract: estimates with aerosol boli. *J. Appl. Physiol.* **64**(3), 1273–1278.

MacRobert T. M. 1948 *Spherical Harmonics*. Dover.

Miki, H., Butler, J. P., Rogers, R. A. & Lehr, J. L. 1993 Geometric hysteresis in pulmonary surface-to-volume ratio during tidal breathing. *J. Appl. Physiol.* **75**, 1630–1636.

Ottino, J. M. 1989 *The Kinematics of Mixing: Stretching, Chaos, and Transport*. Cambridge University Press.

Payne, L. E. 1958 Representation formulas for solutions of a class of partial differential equations. *Tech. Note* B 11–122. Institute for Fluid Dynamics and Applied Mathematics. University of Maryland.

Payne, L. E. & Pell, W. W. 1960 The Stokes flow problem for a class of axially symmetric bodies. *J. Fluid Mech.* **7**, 529–549.

Pozrikidis, C. 1994 Shear flow over a plane wall with an axisymmetric cavity or a circular orifice of finite thickness. *Phys. Fluids* **6**, 68–79.

Rodriguez, M., Bur, S., Favre, A. & Weibel, E. R. 1987 Pulmonary acinus: geometry and morphometry of the peripheral airway system in rat and rabbit. *Am. J. Anat.* **180**, 143–155.

Schneider, J. C., O'niell, M. E. & Brenner, H. 1973 On the slow viscous rotation of a body straddling the interface between two immiscible semi-infinite fluids. *Mathematica* **20**, 175–196.

Schulz, H., Heilmann, P., Hillebrecht, A., Gebhart, J., Meyer, M., Piiper, J. & Heyder, J. 1992 Convective and diffusive gas transport in canine intrapulmonary airways. *J. Appl. Physiol.* **72**, 1557–1562.

Sneddon, I. N. 1972 *The Use of Integral Transforms*. McGraw-Hill.

Taylor, G. I. 1967 Low Reynolds Number Flow, The National Committee for Fluid Mechanics Film, Encyclopaedia Britanica Education Corporation.

Tsuda, A., Butler, J. P. & Fredberg, J. J. 1994*a* Effects of alveolated duct structure on aerosol kinetics. I. Diffusional deposition in the absence of gravity. *J. Appl. Physiol.* **76**, 2497–2509.

Tsuda, A., Butler, J. P. & Fredberg, J. J. 1994*b* Effects of alveolated duct structure on aerosol kinetics. II. Gravitational sedimentation and inertial impaction. *J. Appl. Physiol.* **76**, 2510–2516.

Tsuda, A., Henry, F. S. & Butler, J. P. 1995*a* Chaotic mixing of alveolated duct flow in rhythmically expanding pulmonary acinus. *J. Appl. Physiol.* **79**, 1055–1063.

Tsuda, A., Butler, J. P., Henry, F. S., Otani, Y. & Lehr, J. 1995*b* Chaotic mixing of acinar flow in rhythmically expanding pulmonary acinus (abstract). *Am. J. Respir. Crit. Care Med.* **151**(4), A 232.

Tsuda, A., Otani, Y. & Butler, J. P. 1999 Acinar flow irreversibility caused by perturbations in reversible alveolar wall motion. *J. Appl. Physiol.* **86**, 977–984.

Vuong, S. T. & Sadhal, S. S. 1989 Growth and translation of liquid vapor compound drop in a second liquid. Part 1. Fluid Mechanics. *J. Fluid Mech.* **209**, 617–637.

Watson, E. J. 1974 Fluid flow in a model alveolar sac (Appendix). *J. Appl. Physiol.* **37**, 251.

Weibel, E. R. 1986 Functional morphology of lung parenchyma. In *Handbook of Physiology, The Respiratory System* (ed. A. P. Fishman), Sect. 3, vol III, Chapt. 8, pp. 89–111. Bethesda, MD, Am. Physiol. Soc.

Whittaker, E. T. 1937 *A Treatise on the Analytical Dynamics of Particles and Rigid Bodies*, 4th edn. Cambridge University Press.

Wiggins, S. 1990 *Introduction to Applied Nonlinear Dynamical Systems and Chaos*. Springer.

Zhurina M. I. & Karmazina L. N. 1966 *Tables and Formulas for The Spherical Functions* $P^{m}_{-1/2+i\tau}(z)$. Pergamon.